Journal of Sound and Vibration 329 (2010) 3835–3855

Contents lists available at ScienceDirect

Journal of Sound and Vibration

journal homepage: www.elsevier.com/locate/jsvi

Bifurcations and loss of orbital stability in nonlinear viscoelastic beam arrays subject to parametric actuation

S. Gutschmidt [a,*], O. Gottlieb [b]

[a] Department of Mechanical Engineering, University of Canterbury, Christchurch 8140, New Zealand
[b] Department of Mechanical Engineering, Technion—Israel Institute of Technology, Haifa 32000, Israel

ARTICLE INFO

Article history:
Received 14 January 2010
Received in revised form
26 March 2010
Accepted 26 March 2010
Handling Editor: D.J. Wagg
Available online 18 April 2010

ABSTRACT

The collective dynamic response of microbeam arrays is governed by nonlinear effects, which have not yet been fully investigated and understood. This work employs a nonlinear continuum-based model in order to investigate the nonlinear dynamic behavior of an array of N nonlinearly coupled micro-electromechanical beams that are parametrically actuated. Investigations focus on the behavior of small size arrays in the one-to-one internal resonance regime, which is generated for low or zero DC voltages. The dynamic equations of motion of a two-element system are solved analytically using the asymptotic multiple-scales method for the weakly nonlinear system. Analytically obtained results are verified numerically and complemented by a numerical analysis of a three-beam array. The dynamic responses of the two- and three-beam systems reveal coexisting periodic and aperiodic solutions. The stability analysis enables construction of a detailed bifurcation structure, which reveals coexisting stable periodic and aperiodic solutions. For zero DC voltage only quasi-periodic and no evidence for the existence of chaotic solutions are observed. This study of small size microbeam arrays yields design criteria, complements the understanding of nonlinear nearest-neighbor interactions, and sheds light on the fundamental understanding of the collective behavior of finite-size arrays.

1. Introduction

Micro- and nano-resonators are small flexible electromechanical structures, such as plates, beams and wires that are excited by external electrodynamic or magnetic fields. Arrays of such resonators [1–4] consist of a multitude of coupled elements in configurations where their collective behavior enables a striking enhancement that is not attainable with the individual element performance. In the past decade, microbeam arrays have been successfully used as storage devices [5], as micro-cantilever biosensors [6,7], as opto-mechanical signal processing devices [8], for fast mapping of surfaces via atomic force microscopy [9–11], and recently for protein printing [12]. The dynamic response of these arrays is governed by nonlinear effects [8,1,13–16] which directly influence their performance, but have not yet been fully investigated and understood. The primary focus of microbeam array investigation has been experimental [17,8,12]. To date, documented theoretical models consist of lumped-mass, reduced-order and finite-element approaches. While lumped-mass models [18,14,19] are useful for a qualitative understanding of the system response, it does not resolve the nonlinear spatio-temporal interaction of the individual elements in the array. Finite-element models [9,20], to the other extreme with

* Corresponding author.
E-mail address: stefanie.gutschmidt@canterbury.ac.nz (S. Gutschmidt).

0022-460X/$ - see front matter © 2010 Elsevier Ltd. All rights reserved.
doi:10.1016/j.jsv.2010.03.030

respect to complexity, while adequate for dynamic simulations, are computationally expensive, and do not readily reveal the system's bifurcation structure governed by coexisting stable and unstable solutions. The third approach is that of a reduced-order modeling [21,22] which has gained significant attention for single-element micro-electromechanical systems (MEMS), yet leaves an open amount of fundamental questions when applied to MEMS arrays. While the dynamic behavior of single-resonator MEMS has been studied extensively in literature [23–29],little is known so far for array devices [30,21,8,18] and the collective behavior of interacting members. To the best of our knowledge, no published work to date systematically investigates the complex bifurcation structure of nonlinear MEMS arrays.

Buks and Roukes (BR) [8] employed optical diffraction to study the mechanical properties of an electrically tunable array of suspended doubly-clamped beams which were parametrically excited at primary resonance. The experiments depicted complex multi-valued periodic response for a bias DC voltage range from 0 to 20 V and a very small periodic AC input of 50 mV. Motivated by their work, Lifshitz and Cross (LC) [18] proposed a set of coupled lumped-mass Duffing-type equations of motion for an array excited at its principal parametric resonance and were able to qualitatively explain some of the documented experimental phenomena. Their analytical steady-state asymptotic analysis revealed coexisting stable and unstable periodic solutions for a large bias DC-voltage and a very small AC-voltage excitation. The qualitative agreement between LC and BR includes several abrupt drops in the large size array response as the frequency was swept upwards and downwards.

We note that the data acquisition in BR's experiment [8] did not include a time series but a mean optical measure of intensity that was sampled via a spectrum analyzer. Thus, there is no evaluation of possible coexisting bistable solution or of any possible quasi-periodic or chaotic solution of individual elements in the array. Furthermore, while the analysis of the lumped-mass Duffing array included several coexisting stable and unstable periodic solutions [18], the asymptotic analysis did not reveal, in their slowly varying evolution equations, the existence of any Hopf-related bifurcations that would imply the loss of periodicity culminating with quasi-periodic and chaotic solutions, that have been demonstrated in literature for similar coupled Duffing-like systems [31,32]. However, in a recently performed related study of two coupled nanobeams that were externally excited, Karabalin et al. [33] demonstrated experimentally what appeared to be chaotic like dynamics portrayed by a wide banded spectra and a dense phase plane. They were able to identify parameters of a lumped-mass model based on the equations derived by LC and numerically obtain an excellent comparison with experiment.

In the present work, a dynamical analysis for zero DC voltage is carried out, which reveals an excitation of the system in its one-to-one internal resonance. Investigations are based on a continuum-based nonlinear modal dynamical system. The emphasis is laid on studying the bifurcation structure of small-size arrays, identifying solution types and investigating their stability according to the magnitude of design parameters, such as the grating (that defines the distance between the array elements [34]), a limiting value of input voltage (that will drive two adjacent beams together), and the relationship between linear and nonlinear elastic coefficients (which are not independent [32]). Although the analysis of the present model does not allow for a quantitative comparison to previous experimentally observed results by BR [8], it sheds light on the fundamental understanding of the array behavior and provides significant insights regarding the implementation of future experiments.

The manuscript is organized as follows: In Section 2.1 we formulate the initial-boundary-value problem (IBVP) for the array including both localized nonlinear electrodynamic actuation and dissipation. In the same section the IBVP is reduced to a modal dynamical system via a Galerkin approach which then is investigated analytically in Section 3 employing multiple-scale asymptotics in the vicinity of the system principal parametric resonance. Section 3 also includes stability investigations for the single- and two-beam systems. Numerical validations of the single- and two-beam systems are presented in Section 4.1, followed by numerical simulations of distinct quasi-periodic solutions of the two-beam system in Section 4.2. Section 4.3 presents numerical results of the three-beam system including its frequency response which incorporates periodic as well as distinct aperiodic solutions. This three-element analysis is carried out numerically by means of a numerical continuation method [35,36]. We summarize our findings in Section 5.

2. Model

2.1. Initial-boundary-value problem

We consider an array of N clamped–clamped silicon beams (see Fig. 1). All microbeams (length L, width B, height H, respectively) are assumed to have identical material properties. The equations of motion for a single clamped–clamped

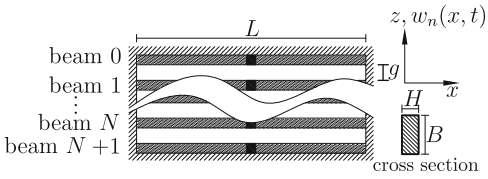

Fig. 1. Definition sketch of the micromechanical array; actuation and dissipative forces applied at midspan of each beam.

nonlinear beam can be found in literature, [32]. We assume a linear stress–strain law and that plane sections remain in the plane. Unlike in BR's experiment, our model considers the electrodynamic interactions as concentrated loads at midspan of each microbeam, which is proportional to the inverse second power of the relative displacement, [34]. Similar to the actuation, we introduce electrodynamical dissipation at midspan of each resonator. Note that the localized parallel plate model employed here is valid for all odd modes of the array elements. The nondimensional field equation of an individual resonator in an array of N beams is

$$w_{n_{\tau\tau}} = Q_n(w_n, w_{n+1}, w_{n-1}, w_{n_\tau}, w_{n+1_\tau}, w_{n-1_\tau}, \tau) - R_n(w_n) - S_n(w_n, w_{n_\tau}), \tag{1}$$

where the length and the time scales are the length of the beam L and the standard frequency $\omega_s^2 = EI/(\varrho AL^4)$, respectively. The actuation term (Q_n) is composed of the electrodynamic actuation (Q_n^E), which is proportional to the quadratic ratio between the input voltage and the relative grating of the array [24,34], and the nonlinear electrodynamic damping force (Q_n^D). Q_n^D is deduced from a quadratic Rayleigh dissipation function [37], which is motivated by experimental observations [8], that reported on a sharp increase in damping with an increase in input voltage. Thus, we assume that damping occurs predominantly as a function of the bias voltage. The restoring force (R_n) is that of a standard Euler–Bernoulli beam with immovable boundary conditions that includes the effect of residual stresses and nonlinear membrane stiffness [32]. We consider here both, a linear viscous and a Kelvin–Voigt visco-elastic damping model [38,39]. The detailed derivations of the dimensional set of equations of motion are presented in [22]. The elastic restoring force R_n, the structural damping force S_n, the generalized dissipation force Q_n^D, and the electrodynamic excitation Q_n^E for each beam are

$$R_n(w_n) = w_{n_{ssss}} + w_{n_{ss}}\left[\kappa_1 - \kappa_3 \int_0^1 w_{n_s}^2 \, \mathrm{d}s\right], \tag{2}$$

$$S_n(w_n, w_{n_\tau}) = \hat{\mu}_1 w_{n_\tau} + \hat{\mu}_2 w_{n_{ssss\tau}}, \tag{3}$$

$$Q_n^D(w_n, w_{n+1}, w_{n-1}, w_{n_\tau}, w_{n+1_\tau}, w_{n-1_\tau}) = \delta\left(s - \frac{1}{2}\right)\hat{\mu}_3 \cdot \left[\frac{(w_{n+1} - w_n)^2 (w_{(n+1)_\tau} - w_{n_\tau})}{(\gamma + w_{n+1} - w_n)^2} - \frac{(w_n - w_{n-1})^2 (w_{n_\tau} - w_{(n-1)_\tau})}{(\gamma + w_n - w_{n-1})^2}\right], \tag{4}$$

$$Q_n^E(w_n, w_{n+1}, w_{n-1}, \tau) = \delta\left(s - \frac{1}{2}\right)\hat{\Gamma} V_{AC}^2 \cos^2\hat{\Omega}\tau \cdot \left[\frac{1}{(\gamma + w_{n+1} - w_n)^2} - \frac{1}{(\gamma + w_n - w_{n-1})^2}\right]. \tag{5}$$

Subscripts in (1)–(5) denote partial derivatives with respect to scaled time τ and the coordinate s along the length of the beam. The nondimensional parameters in (2)–(5) are

$$\hat{\mu}_1 = D_1/(\varrho A\omega_s), \quad \hat{\mu}_2 = D_2/(\varrho A\omega_s L^4), \quad \hat{\mu}_3 = D_3/(\varrho A\omega_s L^2),$$

$$\kappa_1 = N_0 L^2/(EI), \quad \kappa_3 = 6(L/B)^2, \quad \gamma = g/L,$$

$$\hat{\Gamma} = 6\varepsilon_0 L/(EBH^2), \quad \hat{\Omega} = \Omega_{AC}/\omega_s. \tag{6}$$

ε_0, E, I, ρ, A, g, N_0, D_j for j=[1 ..3], and Ω_{AC} are the dimensional quantities: electric constant (vacuum permittivity), Young's modulus, moment of inertia, density, cross sectional area, array grating (gap between resonators), pretensional force, damping coefficients, and excitation frequency, respectively. The nondimensional boundary conditions are $w_n(0,\tau) = 0$, $w_n(1,\tau) = 0$ and $w_{n_s}(0,\tau) = 0$, $w_{n_s}(1,\tau) = 0$ while the first and last beams of the array are prevented from undergoing any motions, i.e. $w_0(s,\tau) = w_{N+1}(s,\tau) = 0$.

2.2. Modal dynamical system

The dynamic response can be approximated in terms of a linear combination of a finite number of orthonormal spatial basis functions with time dependent amplitudes. Thus, the deflections of each microbeam are expressed as the sum of spatial modeshapes with time dependent amplitudes, $w_n(s,\tau) = \sum_{(m)} q_{n,m}(\tau)\Phi_m(s)$, of which the modeshapes $\Phi_m(s)$, which are the eigenmodes associated to the linear undamped homogeneous system of (1), satisfy the b.c. exactly [40,41]. Due to maintained symmetry of the parallel plate model a first-mode discretization captures the nonlinear behavior sufficiently. A brief discussion on this assumption is added in Appendix A. The separation ansatz is substituted into Eqs. (1)–(5) and employing Galerkin's method by multiplication of Φ and integration over the length of the beam (from 0 to 1) yields

$$J_1 q_{n,\tau\tau} + (J_4 + \kappa_1 J_2) q_n - \kappa_3 J_3 q_n^3 + (\hat{\mu}_1 J_1 + \hat{\mu}_2 J_4) q_{n,\tau} = \hat{\mu}_3 \overline{\Phi}^4 \cdot \left[\frac{(q_{n+1} - q_n)^2 (q_{n+1,\tau} - q_{n,\tau})}{(\gamma + q_{n+1}\overline{\Phi} - q_n\overline{\Phi})^2} - \frac{(q_n - q_{n-1})^2 (q_{n,\tau} - q_{n-1,\tau})}{(\gamma + q_n\overline{\Phi} - q_{n-1}\overline{\Phi})^2}\right]$$
$$+ \overline{\Phi}\hat{\Gamma} V_{AC}^2 \cos^2\hat{\Omega}\tau \left[\frac{1}{(\gamma + q_{n+1}\overline{\Phi} - q_n\overline{\Phi})^2} - \frac{1}{(\gamma + q_n\overline{\Phi} - q_{n-1}\overline{\Phi})^2}\right], \tag{7}$$

with $\overline{\Phi} = \Phi(1/2)$ and

$$J_1 = \int_0^1 \Phi^2 \, \mathrm{d}s, \quad J_2 = \int_0^1 \Phi\Phi_{ss} \, \mathrm{d}s,$$

$$J_3 = \int_0^1 \Phi\Phi_{ss}\left[\int_0^1 (\Phi_s)^2 \, \mathrm{d}s\right] \mathrm{d}s, \quad J_4 = \int_0^1 \Phi\Phi_{ssss} \, \mathrm{d}s = z_1^4 J_1.$$

We rescale the resulting ordinary differential equations by $x_n = \overline{\Phi} q_n/\gamma$ and $t^* = z_1^2\tau$ ($z_1 \approx 4.73$ for $\kappa_1 = 0$) to yield the final modal dynamical system:

$$\ddot{x}_n + \alpha x_n + \beta x_n^3 + \mu_L \dot{x}_n - \tilde{\mu}_{NL}\left[\frac{(x_{n+1}-x_n)^2(\dot{x}_{n+1}-\dot{x}_n)}{(1+x_{n+1}-x_n)^2} - \frac{(x_n-x_{n-1})^2(\dot{x}_n-\dot{x}_{n-1})}{(1+x_n-x_{n-1})^2}\right] = \eta_{AC}^2 \cos^2\Omega t^* \left[\frac{1}{(1+x_{n+1}-x_n)^2} - \frac{1}{(1+x_n-x_{n-1})^2}\right], \tag{8}$$

whereas parameters are defined as

$$\alpha = 1 - \frac{\kappa_1 |J_2|}{J_1 z_1^4}, \quad \beta = \frac{\kappa_3 \gamma^2}{z_1^4 \overline{\Phi}^2}\frac{|J_3|}{J_1},$$

$$\mu_L = \frac{\hat{\mu}_1}{z_1^2} + \frac{\hat{\mu}_2 J_4}{z_1^2 J_1}, \quad \tilde{\mu}_{NL} = \frac{\hat{\mu}_3 \overline{\Phi}^2}{J_1 z_1^2},$$

$$\eta_{AC}^2 = \hat{\Gamma}^* V_{AC}^2, \quad \hat{\Gamma}^* = \frac{\hat{\Gamma}\overline{\Phi}^2}{\gamma^3 J_1 z_1^4}, \quad \Omega = \frac{\hat{\Omega}}{z_1^2}.$$

Derivatives in (8) are with respect to t^*. The gap parameter γ appears in the parameters of cubic stiffness β and excitation η_{AC}. The actuation term $\eta_{AC}^2 \cos^2\Omega t^*$ in (8) can be rewritten as $\eta_{AC}^2(1+\cos(2\Omega t^*))/2$ of which the harmonic part reveals the parametric excitation. Thus, the principal and fundamental parametric resonance frequencies occur at $\Omega = \sqrt{\alpha}$ and $\Omega = \sqrt{\alpha}/2$, respectively. We note that the dynamical system in (8) readily reduces to the coupled Duffing-like system proposed by LC [18] with the IBVP derivation revealing coupling between parameters.

3. Asymptotic analysis

3.1. Single-beam system

Considerable work has been done for the single-beam system under the same [41] or similar [42] electrode configuration as studied in this work. However, we include the analysis of the single-beam system for the sake of completion. The equations of motion for the single-beam system, given in (8), reduce to

$$\ddot{x} + \alpha x + \beta x^3 + \mu_L \dot{x} + \mu_{NL}\frac{x^2(1+x^2)}{(1-x^2)^2}\dot{x} = \frac{1}{2}\eta^2(1+\cos 2\Omega t^*)\frac{x}{(1-x^2)^2} \tag{9}$$

in which, and henceforth, the following parameters are redefined to $\mu_{NL} = 2\tilde{\mu}_{NL}$ and $\eta = 2\eta_{AC}$. Before carrying out the asymptotic multiple-scales method, (9) is pre-multiplied by the denominator of the forcing term. The dynamical response of the beam is represented by three different time scales that are distinguished by the small parameter ε. Scales and small parameters for the multiple-scales technique have to be chosen according to parameter and resonance regions of the system. Considering the dynamical analysis carried out in the one-to-one internal resonance region (small to zero DC voltage), the alternating AC-voltage parameter can take on larger values. However, it is still assumed to be a small parameter of order ε and thus, $\eta = \varepsilon\overline{\eta}$. Furthermore, the linear damping coefficients in MEMS devises (in general) are usually low due to large quality factors. Therefore also the linear damping parameter is treated as a small parameter, $\mu_L = \varepsilon^2\overline{\mu}_L$. Due to low damping and excitation the solution can be decomposed into fast- and slow-varying components. The contribution of nonlinear terms in (9), which are assumed to be small, causes a deviation from the solution of the purely linear problem. This deviation is expressed by a variation of the amplitude and phase based on the slow time scale $T_2 = \varepsilon^2 t^*$. The displacement is extended into a power series in ε: $x = \sum_{j=1}^{3} \varepsilon^j x_j(T_0, T_1, T_2, \ldots) + O(\varepsilon^4)$. The coefficients of each order of ε are collected and form the following set of equations:

$$O(\varepsilon^1): \quad D_0^2 x_1 + \omega^2 x_1 = 0, \tag{10}$$

$$O(\varepsilon^2): \quad D_0^2 x_2 + \omega^2 x_2 = -2D_0 D_1 x_1, \tag{11}$$

$$O(\varepsilon^3): \quad D_0^2 x_3 + \omega^2 x_3 = -2D_0 D_1 x_2 - D_1^2 x_1 - 2D_0 D_2 x1 - \beta x_1^3 - \overline{\mu}_L D_0 x_1 - \mu_{NL} x_1^2 D_0 x_1 + 2x_1^2(D_0^2 x_1 + \omega^2 x_1) + \frac{1}{2}\overline{\eta}^2(1+\cos(2\Omega t^*))x_1 \tag{12}$$

with $\omega^2=\alpha$. The derivatives D_m for m=[0 . .2] are defined as $D_m=\partial/\partial T_m$. The solution of the $O(\varepsilon^1)$ equation is

$$x_1=A(T_1,T_2)\exp(\mathrm{i}\omega T_0)+\overline{A}(T_1,T_2)\exp(-\mathrm{i}\omega T_0). \tag{13}$$

Substitution of (13) into (11) leads to $D_1A(T_1,T_2)$=0 which means that A is independent of the time scale T_1. The particular solution of (11) vanishes and the homogeneous solution is identical to the solution of (10), i.e. x_2=x_1. Substitutions of solutions x_1 and x_2 into (12) with D_1x_1=D_1x_2=0 yield

$$\begin{aligned}D_0^2x_3+\omega^2x_3=&\left[-\mathrm{i}\omega(2D_2A+\overline{\mu}_LA+\mu_{NL}A^2\overline{A})-3\beta A^2\overline{A}+\frac{1}{2}\overline{\eta}^2A+\frac{1}{4}\overline{\eta}^2\overline{A}\exp(2\mathrm{i}\sigma T_1)\right]\exp(\mathrm{i}\omega T_0)\\&+\left[-\beta A^3-\mathrm{i}\omega\mu_{NL}A^3+\frac{1}{4}\overline{\eta}^2A\exp(2\mathrm{i}\sigma T_1)\right]\exp(3\mathrm{i}\omega T_0)+\mathrm{cc.},\end{aligned} \tag{14}$$

where the detuning is $\varepsilon^2\sigma=\Omega-\omega$ and cc. represents the conjugate complex part of the above presented terms. Elimination of secular terms in (14) yields

$$-\mathrm{i}\omega(2D_2A+\overline{\mu}_LA+\mu_{NL}A^2\overline{A})-3\beta A^2\overline{A}+\frac{1}{2}\overline{\eta}^2A+\frac{1}{4}\overline{\eta}^2\overline{A}\exp(2\mathrm{i}\sigma T_1)=0. \tag{15}$$

Substituting the polar coordinates $A=a\exp(\mathrm{i}\theta)/2$ into (15) and separating imaginary and real terms results in the following slowly varying evolution equations

$$a'=\left(\frac{1}{2}\delta_{\mathrm{ex}}\sin2\psi-\zeta_L\right)a-\zeta_{NL}a^3, \tag{16}$$

$$a\psi'=\left(\frac{1}{2}\delta_{\mathrm{ex}}\cos2\psi+\sigma+\delta_{\mathrm{ex}}\right)a-\frac{1}{2}\delta_3a^3, \tag{17}$$

with $\psi=2\sigma T_2-2\theta$, $\zeta_L=\overline{\mu}_L/2$, $\zeta_{NL}=\mu_{NL}/8$, $\delta_{\mathrm{ex}}=\overline{\eta}^2/(4\omega)$ and $\delta_3=3\beta/(4\omega)$. Derivatives in (16) and (17) are with respect to T_2.

In steady-state operation any changes with respect to time vanish, i.e. a' and ψ' in (16) and (17) are equal to zero. One solution of (16) and (17) is the trivial solution a=0. In order to find the solutions for the nontrivial case the harmonic terms in (16) and (17) are eliminated by solving the equations of the same, respectively, then squaring each of the equation and adding them, which results in

$$\delta_{\mathrm{ex}}^2=(2\zeta_L+2\zeta_{NL}a^2)^2+(\delta_3a^2-2\sigma-2\delta_{\mathrm{ex}})^2. \tag{18}$$

Multiplying (18) by ε^4 and re-substituting unscaled parameters and detuning $\varepsilon^2\sigma=\Omega-\omega$ yields the frequency response function ($\varepsilon a=\varepsilon a(\Omega)$):

$$\Omega_{1,2}=\frac{1}{2}\delta_3\varepsilon^2a^2-\frac{\eta^2}{4\omega}\pm\frac{1}{2}\sqrt{\frac{\eta^4}{16\omega^2}-\left(\mu_L+\frac{\mu_{NL}}{4}\varepsilon^2a^2\right)^2}+\omega. \tag{19}$$

Detailed steps for deriving (19) from (18) can be found in Appendix B. Fig. 2 depicts the hardening frequency response characteristic for the given set of parameters $\alpha=2.8982$, $\beta=11.5091$, Q=500, $\mu_{NL}=0.6$, and $\eta=0.1636$, which corresponds to the turning point of the m_2=0 curve in the stability diagram in Fig. 3b (marked by the dashed line). Although much

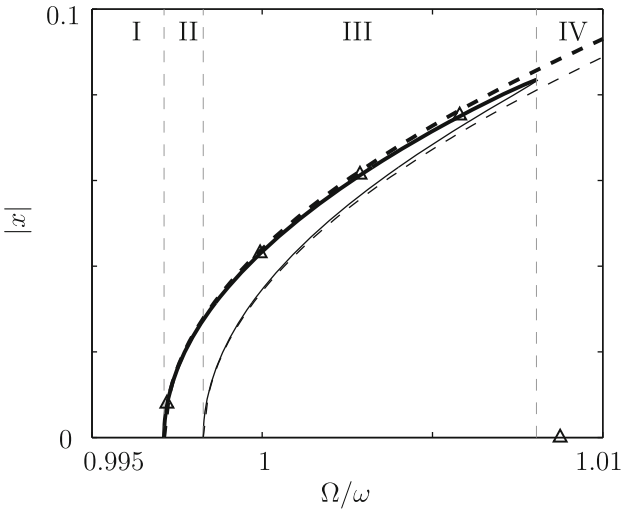

Fig. 2. Frequency response characteristic of the single-beam system; $\alpha=2.8982$, $\beta=11.5091$, Q=500, $\eta=0.1636$, thick lines: stable, thin lines: unstable, solid lines: $\mu_{NL}=0.6$, dashed lines: $\mu_{NL}=0$, triangles: numerical verifications.

higher quality factors can occur in MEMS devices, a quality factor of Q=500 is chosen for all simulations in this paper in order to allow for a relatively fast vanishing of transient oscillations, especially for quasi- and aperiodic vibration responses. For the nonlinear damping parameter equal to zero, the curves do not close and thus amplitudes become infinite. The stability of the nontrivial steady-state solutions is determined by analyzing the eigenvalue problem of the Jacobian of the system (Eqs. (16) and (17)) for $\mu_{NL}=0$. The characteristic equation is $\lambda^2+m_1\lambda+m_2=0$ with $m_1=\mu_L>0$ and $m_2=\varepsilon a^2\delta_3(-2(\Omega-\omega)-2\eta^2/\omega+\delta_3\varepsilon a^2)$. The trivial solution is stable in regions I and III (+IV), see Fig. 2. The upper branch in Fig. 2, presented by the solid line, is stable while the lower (dashed line) is unstable. Fig. 3 presents the stability criteria of the nontrivial steady-state solutions of the single-beam system for $\mu_{NL}=0$. The horizontal grey dashed-dashed line represents the AC-value for which the response in Fig. 2 is portrayed.

There exists a critical excitation value (η- threshold) for which the amplitude square a^2 is equal to zero. Below this value there is no solution other than the trivial solution. This η- value is presented by the dashed-dotted lines in Fig. 3. The solid (Fig. 3a) and the dashed lines (Fig. 3b) present the critical lines m_2=0, respectively. They are identical to the threshold beyond which the amplitudes become negative.

3.2. Two-beam system

The equations of motion for a two-beam array in (8) reduce to

$$\ddot{x}_1+\alpha x_1+\beta x_1^3+\mu_L\dot{x}_1-\tilde{\mu}_{NL}\left[\frac{(x_2-x_1)^2(\dot{x}_2-\dot{x}_1)}{(1+x_2-x_1)^2}-\frac{x_1^2\dot{x}_1}{(1+x_1)^2}\right]=\frac{1}{2}\eta_{AC}^2(1+\cos2\Omega t^*)\left[\frac{1}{(1+x_2-x_1)^2}-\frac{1}{(1+x_1)^2}\right], \tag{20}$$

$$\ddot{x}_2+\alpha x_2+\beta x_2^3+\mu_L\dot{x}_2-\tilde{\mu}_{NL}\left[\frac{(-x_2)^2(-\dot{x}_2)}{(1-x_2)^2}-\frac{(x_2-x_1)^2(\dot{x}_2-\dot{x}_1)}{(1+x_2-x_1)^2}\right]=\frac{1}{2}\eta_{AC}^2(1+\cos2\Omega t^*)\left[\frac{1}{(1-x_2)^2}-\frac{1}{(1+x_2-x_1)^2}\right]. \tag{21}$$

In analogy to the single-beam system Eqs. (20) and (21) are pre-multiplied by the denominator of the forcing terms, respectively. The method of multiple scales is applied again, whereas the displacements for the two beams are $x_n=\sum_{j=1}^{3}\varepsilon^j x_{nj}(T_0,T_1,T_2,\ldots)+O(\varepsilon^4)$. The same scaling for the linear damping coefficient and the AC-voltage parameter as in the case of the single-beam system is applied. Substitution of the solution form, including the scaling of the AC-parameter and the linear damping coefficient and then collecting the terms of different orders in ε, results in the following set of equations:

$$O(\varepsilon^1): \quad D_0^2x_{n1}+\omega^2x_{n1}=0, \tag{22}$$

$$O(\varepsilon^2): \quad D_0^2x_{n2}+\omega^2x_{n2}=f_{n2}, \tag{23}$$

$$O(\varepsilon^3): \quad D_0^2x_{n3}+\omega^2x_{n3}=f_{n3}, \tag{24}$$

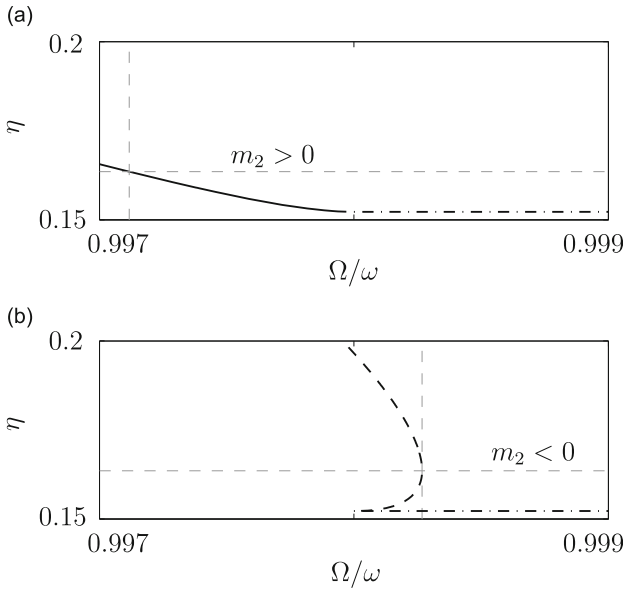

Fig. 3. Stability diagram of the nontrivial solution of the single-beam system; (a) stability regions for upper branch, (b) stability regions for lower branch; dash-dotted lines: AC-threshold, grey dashed lines: marker for $\eta=0.1636$ (Fig. 2).

with $\omega^2=\alpha$ and

$$f_{n2}=-2D_0D_1x_{n1}-2x_{m1}(D_0^2x_{n1}+\alpha x_{n1}), \tag{25}$$

$$\begin{aligned}f_{n3}=&-D_1^2x_{n1}-2D_0D_2x_{n1}-2D_0D_1x_{n2}-\beta x_{n1}^3-\overline{\mu}_L D_0x_{n1}+(-1)^n2x_{m1}(2D_0D_1x_{11}+D_0^2x_{n2}+\alpha x_{n2})\\&+(-x_{m1}^2+2x_{n1}^2-2x_{11}x_{21}+(-1)^n2x_{m2})\cdot(D_0^2x_{n1}+\alpha x_{n1})-(-1)^n\mu_{NL}(-x_{m1}^2(D_0x_{11}-D_0x_{21})\\&+2x_{11}x_{21}(D_0x_{11}-D_0x_{21})+(-1)^nx_{n1}^2(2D_0x_{n1}-D_0x_{m1}))+\frac{1}{2}\overline{\eta}^2(1+\cos2\Omega t^*)\cdot(2x_{n1}-x_{m1}),\end{aligned} \tag{26}$$

where $m=-1^{n+1}+n$. Note that the occurrences of the terms containing $D_0^2x_{n1}+\alpha x_{n1}$ (n=[1,2]), respectively, on the right-hand side of Eqs. (23) and (24) have their origin in the pre-multiplication of the denominators of the forcing terms in Eqs. (20) and (21). Such terms exhibit the terms involved in the same technique but, instead of a pre-multiplication of the denominator, having expanded the forcing terms into a Taylor series.

A single mode representation of the solution

$$x_{n1}=A_n(T_1,T_2)\exp(\mathrm{i}\omega T_0)+\overline{A}_n(T_1,T_2)\exp(-\mathrm{i}\omega T_0) \tag{27}$$

is chosen, which upon substitution into (23) leads to

$$D_0^2x_{n2}+\omega^2x_{n2}=-2\mathrm{i}\omega D_1A_n(T_1,T_2)\exp(\mathrm{i}\omega T_0)+\mathrm{cc}. \tag{28}$$

The only secular terms in (28) are $-2\mathrm{i}\omega D_1A_n$ for n=[1,2], respectively. All other (nonsecular) terms cancel out. D_1A_n=0 in (28) mean that the $A_n(T_1,T_2)$ are independent of the time scale T_1 and thus terms in (24) containing D_1^n vanish. Furthermore, the solution of (23) is equal to the solution of (22), and thus $x_{n\,2}=x_{n\,1}$. The detuning remains the same as in the case of the single-beam system. Substitutions of solutions $x_{n\,1}$ and $x_{n\,2}$ into (24) and elimination of secular terms yield the following slowly varying complex evolution equations:

$$\begin{aligned}&-2\mathrm{i}\omega D_2A_1+\frac{1}{2}\mathrm{i}\omega\mu_{NL}A_1^2\overline{A}_2-\frac{1}{4}\overline{\eta}^2A_2-\left(\overline{\mu}_L\mathrm{i}\omega-\frac{1}{2}\overline{\eta}^2\right)A_1+\frac{1}{4}\overline{\eta}^2\exp(\mathrm{i}2\sigma T_2)\overline{A}_1+\mu_{NL}\mathrm{i}\omega A_1\overline{A}_1A_2+\frac{1}{2}\mu_{NL}\mathrm{i}\omega A_2^2\overline{A}_2-\mu_{NL}\mathrm{i}\omega A_1A_2\overline{A}_2\\&-\frac{1}{2}\mu_{NL}\mathrm{i}\omega A_2^2\overline{A}_1-(3\beta+\mu_{NL}\mathrm{i}\omega)A_1^2\overline{A}_1-\frac{1}{8}\overline{\eta}^2\exp(\mathrm{i}2\sigma T_2)\overline{A}_2=0\end{aligned} \tag{29}$$

and

$$\begin{aligned}&-2\mathrm{i}\omega D_2A_2-\frac{1}{2}\mathrm{i}\omega\mu_{NL}A_1^2\overline{A}_2-\frac{1}{4}\overline{\eta}^2A_1-\left(\overline{\mu}_L\mathrm{i}\omega-\frac{1}{2}\overline{\eta}^2\right)A_2+\frac{1}{4}\overline{\eta}^2\exp(\mathrm{i}2\sigma T_2)\overline{A}_2+\mu_{NL}\mathrm{i}\omega A_1A_2\overline{A}_2+\frac{1}{2}\mu_{NL}\mathrm{i}\omega A_2^2\overline{A}_1-\mu_{NL}\mathrm{i}\omega A_1A_2\overline{A}_1\\&+\frac{1}{2}\mu_{NL}\mathrm{i}\omega A_1^2\overline{A}_1-(3\beta+\mu_{NL}\mathrm{i}\omega)A_2^2\overline{A}_2-\frac{1}{8}\overline{\eta}^2\exp(\mathrm{i}2\sigma T_2)\overline{A}_1=0.\end{aligned} \tag{30}$$

Substituting the polar coordinates $A_n=a_n\exp(\mathrm{i}\theta_n)/2$ into Eqs. (29) and (30) and separating imaginary and real terms yields the set of slowly varying evolution equations

$$a_1'=\zeta_{NL}\left[-a_1^3+\left(\frac{1}{2}+\cos\psi_1\right)a_1^2a_2-\left(1+\frac{1}{2}\cos\psi_1\right)a_1a_2^2+\frac{1}{2}\cos\psi_1\,a_2^3\right]-\left[\zeta_L+\frac{1}{2}\,\delta_{\mathrm{ex}}\sin(\psi_1-\psi_2)\right]a_1+\frac{1}{2}\,\delta_{\mathrm{ex}}\left(\sin\psi_1-\frac{1}{2}\sin\psi_2\right)a_2, \tag{31}$$

$$a_1(\psi_1'-\psi_2')=\delta_3\;a_1^3-\zeta_{NL}\sin\psi_1[2a_1^2a_2-a_1a_2^2+a_2^3]-2\left[\delta_{\mathrm{ex}}\left(1+\frac{1}{2}\cos(\psi_1-\psi_2)\right)+\sigma\right]a_1+\delta_{\mathrm{ex}}\left(\cos\psi_1+\frac{1}{2}\cos\psi_2\right)a_2, \tag{32}$$

$$a_2'=\zeta_{NL}\left[\frac{1}{2}\cos\psi_1a_1^3-\left(1+\frac{1}{2}\cos\psi_1\right)a_1^2a_2+\left(\frac{1}{2}+\cos\psi_1\right)a_1a_2^2-a_2^3\right]-\frac{1}{2}\,\delta_{\mathrm{ex}}\left(\sin\psi_1+\frac{1}{2}\sin\psi_2\right)a_1+\left[-\zeta_L+\frac{1}{2}\delta_{\mathrm{ex}}\sin(\psi_1+\psi_2)\right]a_2, \tag{33}$$

$$a_2(\psi_1'+\psi_2')=-\zeta_{NL}\sin\psi_1[a_1^3-a_1^2a_2+2a_1a_2^2]-\delta_{\mathrm{ex}}\left(\cos\psi_1+\frac{1}{2}\cos\psi_2\right)a_1-\delta_3a_2^3+2\left[\delta_{\mathrm{ex}}\left(1+\frac{1}{2}\cos(\psi_1+\psi_2)\right)+\sigma\right]a_2, \tag{34}$$

where $\psi_1=\theta_1-\theta_2$ and $\psi_2=2\sigma T_2-\theta_1-\theta_2$ and δ_3, δ_{ex}, ζ_L and ζ_{NL} as defined previously.

Fixing one of the beams by setting either a_1 or a_2 equal to zero, results in a set of two equations which are identical to the set of equations of the single-beam system (cf. (16) and (17)). Steady state is deduced from Eqs. (31)–(34) by setting a_n' and ψ_n' (n=1,2) equal to zero. There exist three nontrivial solutions for the two-beam system in addition to the trivial solution (a_1=a_2=0):

(i) The first nontrivial solution is derived from the case when both beams vibrate in-phase and with same amplitudes, a_1=a_2. The phase angle $\psi_1=\theta_1-\theta_2$ becomes $0+2k\pi$ (k is an integer). a and ψ correspond to either of the beams and thus denote a_n and $\psi_2=2\sigma T_2-2\theta_n$. a_1=a_2=a satisfies Eqs. (31)–(34) along with

$$\sin\psi_1=0,\quad \cos\psi_1=1,$$

$$\sin\psi_2=2\frac{\zeta_{NL}a^2+2\zeta_L}{\delta_{\mathrm{ex}}},\quad \cos\psi_2=2\frac{\delta_3a^2-2\sigma-\delta_{\mathrm{ex}}}{\delta_{\mathrm{ex}}}.$$

Substitution of this solution into (31) results in the amplitude–frequency relationship for the in-phase (IP) case

$$\delta_{ex}^2 = (4\zeta_L + 2\zeta_{NL}a^2)^2 + (2\delta_3 a^2 - 4\sigma - 2\delta_{ex})^2. \tag{35}$$

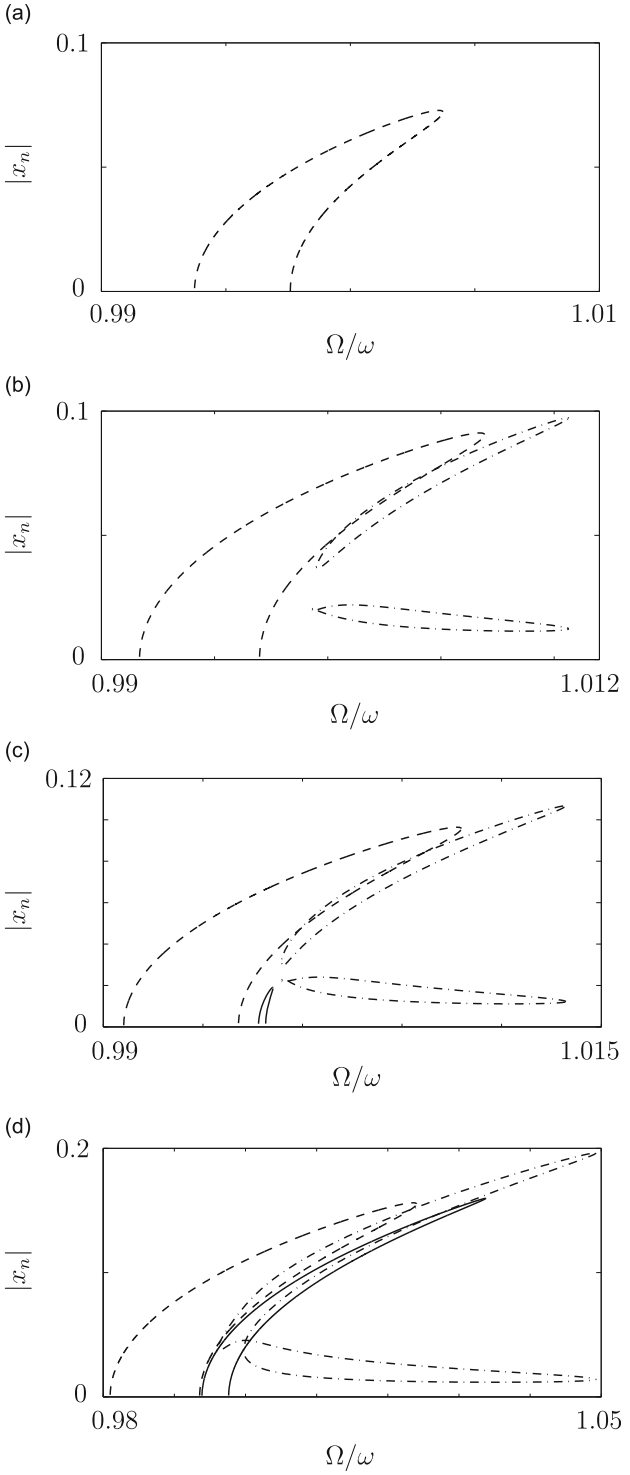

Fig. 4. Frequency response characteristics for the two-beam system; dashed lines: OOP ($x_1 = -x_2$), solid lines: IP ($x_1 = x_2$), dash-dotted lines: IP ($x_1 \neq x_2$); $\alpha = 2.8982$, $\beta = 11.5091$, $Q = 500$, $\mu_{NL} = 2.4$; (a) $\eta = 0.1831$, (b) $\eta = 0.2092$, (c) $\eta = 0.2171$, (d) $\eta = 0.3138$.

(ii) The second steady-state solution is deduced from the case when both beams vibrate with the same amplitude but out-of-phase. The phase angle $\psi_1 = \theta_1 - \theta_2$ then becomes $\pi + 2k\pi$. This along with

$$a_1 = a_2 = a, \quad \sin\psi_1 = 0, \quad \cos\psi_1 = -1,$$

$$\sin\psi_2 = -\frac{2}{3}\frac{5\zeta_{NL}a^2 + 2\zeta_L}{\delta_{ex}}, \quad \cos\psi_2 = -\frac{2}{3}\frac{\delta_3 a^2 - 2\sigma - 3\delta_{ex}}{\delta_{ex}}$$

satisfies Eqs. (31)–(34). Substitution of this solution into (31) results in the amplitude–frequency relationship for the out-of-phase (OOP) case

$$9\delta_{ex}^2 = (4\zeta_L + 10\zeta_{NL}a^2)^2 + (2\delta_3 a^2 - 4\sigma - 6\delta_{ex})^2. \tag{36}$$

(iii) The third steady-state solution is found by solving the algebraic set of equations (deduced from Eqs. (31)–(34)) numerically. This solution incorporates unequal amplitudes ($a_1 \neq a_2$) and corresponds to an in-phase mode.

The IP (35) and OOP (36) solutions are biquadratic equations in a, respectively. The condition for which the amplitude square, a^2, is greater than zero is determined from solutions (35) and (36), respectively, by differentiating the same with respect to σ and setting $da/d\sigma$ equal to zero. Substituting the local extremum σ_E into (35) and (36), and solving

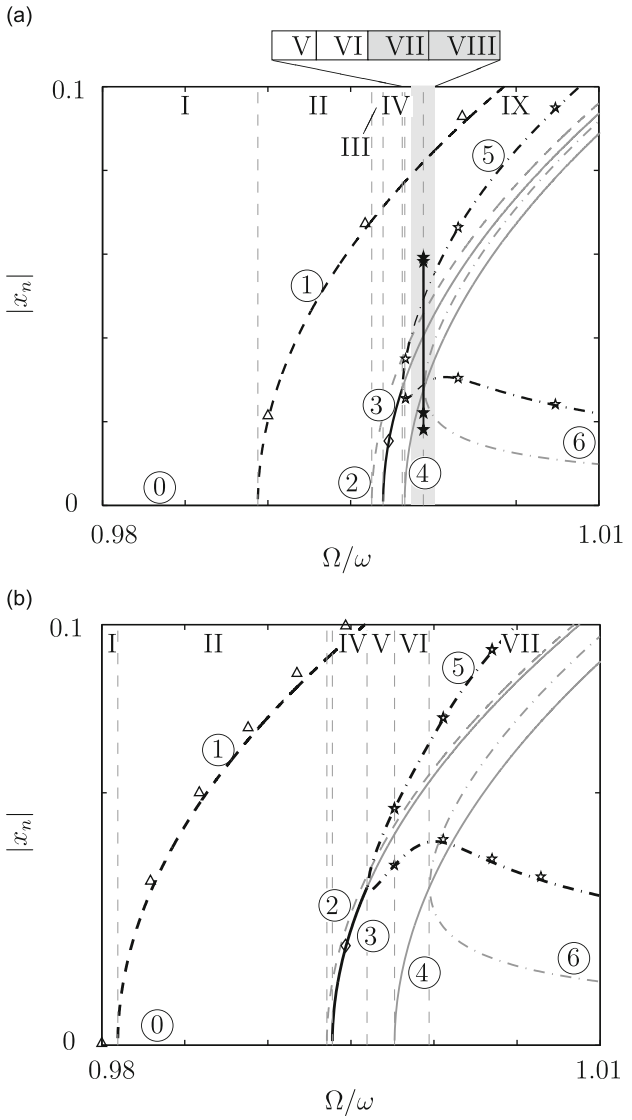

Fig. 5. Frequency response characteristic for the two-beam system; $\alpha = 2.8982$, $\beta = 11.5091$, Q=500, $\mu_{NL} = 0$; (a) $\eta = 0.2354$, (b) $\eta = 0.3138$; bold black lines: stable, thin grey lines: unstable, markers denote numerical simulations, hollow: periodic response, solid: quasi-periodic response, diamonds and stars: IP, triangles: OOP; solutions: (0) trivial (indicated but not explicitly shown), (1), (2) OOP, (3), (4) and (5), (6) IP.

for a^2 yields

$$a^2_{\min} \geq \frac{\delta_{ex}-4\zeta_L}{2\zeta_3} \quad \text{(IP)} \quad \text{and} \tag{37}$$

$$a^2_{\min} \geq \frac{3\delta_{ex}-4\zeta_L}{10\zeta_3} \quad \text{(OOP)}. \tag{38}$$

A step-by-step derivation of (37) and (38) can be found in Appendix C. Thus, (37) and (38) yield the conditions for the lower bounds of the AC-voltage:

$$\eta \geq \sqrt{\frac{8}{Q}}\omega \quad \text{(IP)} \quad \text{and} \tag{39}$$

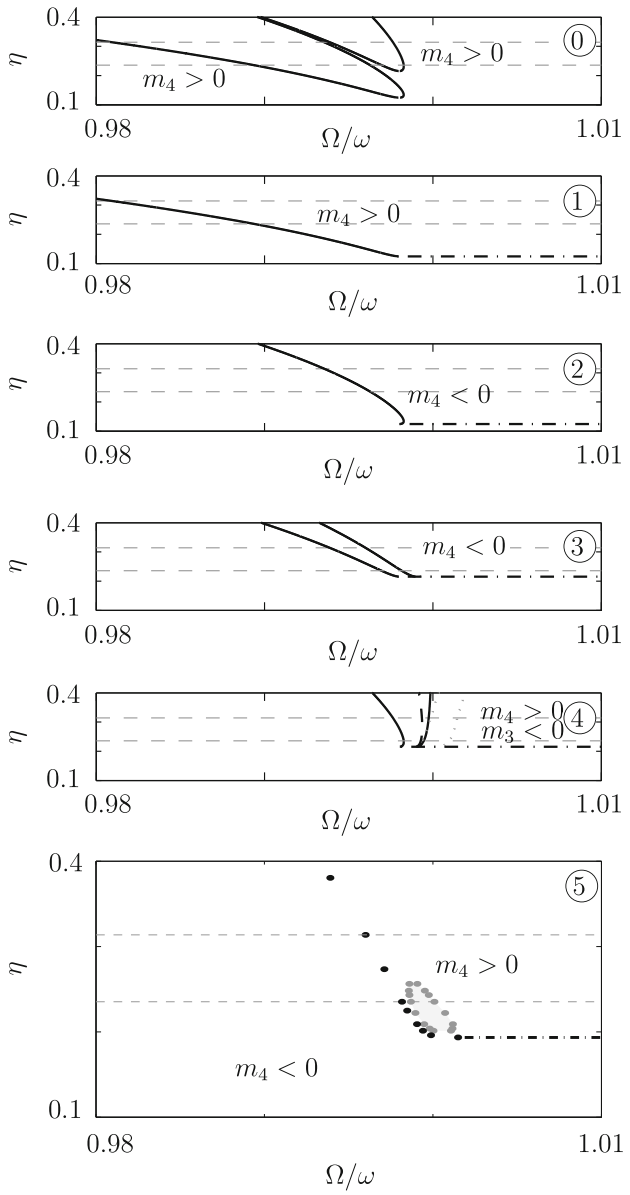

Fig. 6. Stability map for the solution branches of the two-beam system (0)–(5) (see Fig. 5); bold solid lines and bold black dots: m_4=0, bold dash-dotted lines: AC-threshold for existing solutions, black dashed line: m_3=0, grey dotted lines and grey bold dots: Hopf criteria $\Delta_3 = m_3(m_1m_2-m_0m_3)-m_1^2m_4 = 0$, shaded area: Hopf isle ($\Delta_3 < 0$), grey dashed lines: markers for $\eta = 0.2354$ and 0.3138.

$$\eta \geq \sqrt{\frac{8}{3Q}}\omega \quad \text{(OOP)}. \tag{40}$$

For a Q-factor of Q=500 AC-thresholds obtained from (39) and (40) are $\eta = 0.2153$ (IP) and $\eta = 0.1243$ (OOP), respectively. The AC-threshold of the solution for which the two beams vibrate in-phase with unequal amplitudes is determined numerically to be $\eta = 0.1935$.

Fig. 4 presents all three nontrivial steady-state solutions for the given set of parameters $\alpha = 2.8982$, $\beta = 11.5091$, Q=500, $\mu_{NL} = 2.4$, and four different AC-voltage values. Fig. 4a shows the frequency response of the two-beam system for an AC-value above the OOP-mode and below the IP-mode thresholds ($0.1243 < \eta < 0.1935$) and thus, the two IP solutions do not appear. The dynamic response in Fig. 4b is plotted for an AC-voltage parameter between the two IP-mode thresholds ($0.1935 < \eta < 0.2153$) and thus, the IP solution with unequal amplitudes exists while the other with equal amplitudes does

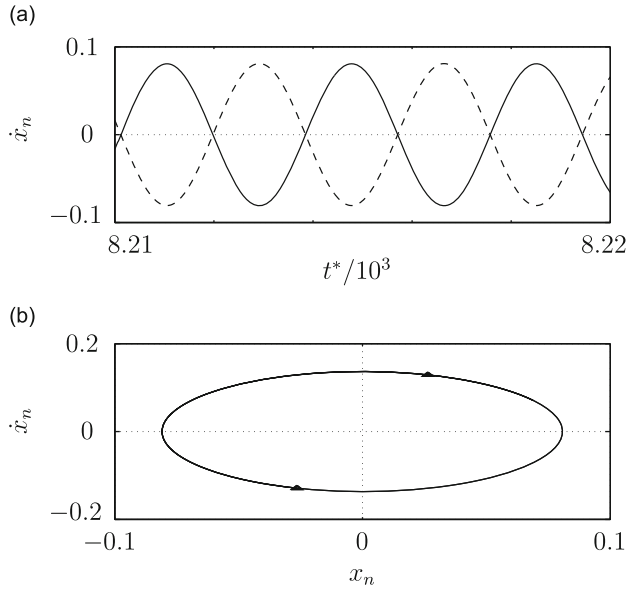

Fig. 7. Simulation in region II of Fig. 5b ($\Omega = 0.99\omega$); (a) time series, solid line: x_1, dashed line: x_2, (b) phase plane with Poincaré points, solid line: $\dot{x}_1 - x_1$- plane, dashed line: $\dot{x}_2 - x_2$- plane, triangles: Poincaré points.

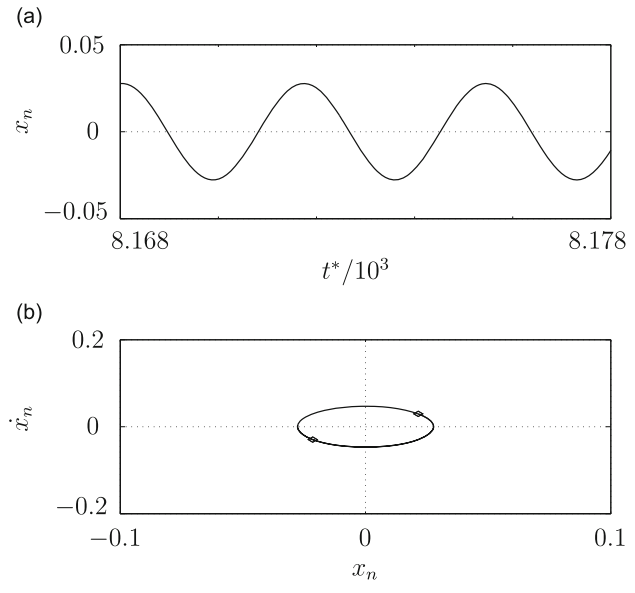

Fig. 8. Simulation in region IV of Fig. 5b ($\omega = 0.995\omega$); (a) time series, solid line: x_1, dashed line: x_2 (b) phase plane with Poincaré points, solid line: $\dot{x}_1 - x_1$- plane, dashed line: $\dot{x}_2 - x_2$- plane (identical and thus invisible), diamonds: Poincaré points.

not. In Fig. 4c and d, which are plotted for AC-values above all thresholds, all solutions, OOP and two IP, exist. Note that up to another critical AC-value, the IP solution with unequal amplitudes includes two separate closed branches. Only for values of $\eta = 0.2236$ and above the characteristic curves are joined to yield continuous branches. Fig. 5 depicts the three steady-state solutions for $\alpha = 2.8982$, $\beta = 11.5091$, Q=500, $\mu_{NL} = 0$ and (a) $\eta = 0.2354$ and (b) $\eta = 0.3138$, including the OOP (branches (1) and (2)), and the two IP solutions (branches (3), (4) and (5), (6)).

In the following we investigate in the stability of the solutions in each region of Fig. 5. Stability analysis is carried out for the system with zero nonlinear damping ($\mu_{NL} = 0$). The nonlinear damping closes the curves and thus sets a bound to the maximum amplitudes. However, in the bifurcation domain the influence of the nonlinear damping with respect to the bifurcation structure occurs to be small. Zero nonlinear damping allows for a formulation of the stability criteria in closed form. Eqs. (31)–(34) are rewritten into the form $\xi' = f(\xi)$ with $\xi = [a_1, \psi_1, a_2, \psi_2]^{\mathrm{T}}$. Stability analysis of the trivial steady-state solution is done using the Cartesian form of Eqs. (31)–(34), whereas stability of the nontrivial steady-state solutions make use of the polar form. The eigenvalue problem for the Jacobian of the system is analyzed using the quartic characteristic equation $\lambda^4 + m_1\lambda^3 + m_2\lambda^2 + m_3\lambda + m_4 = 0$, where m_1 is always greater than zero for all solution branches throughout all regions. Fig. 6 depicts the bifurcation characteristics of the AC-voltage parameter η over the scaled

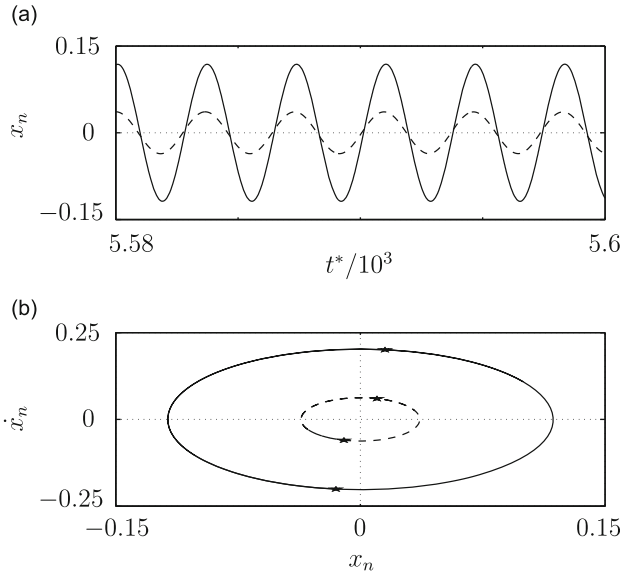

Fig. 9. Simulation in region VII of Fig. 5b ($\omega = 1.01\omega$); (a) time series, solid line: x_1, dashed line: x_2 (b) phase plane with Poincaré points, solid line: $\dot{x}_1 - x_1$-plane, dashed line: $\dot{x}_2 - x_2$- plane (identical and thus invisible), diamonds: Poincaré points.

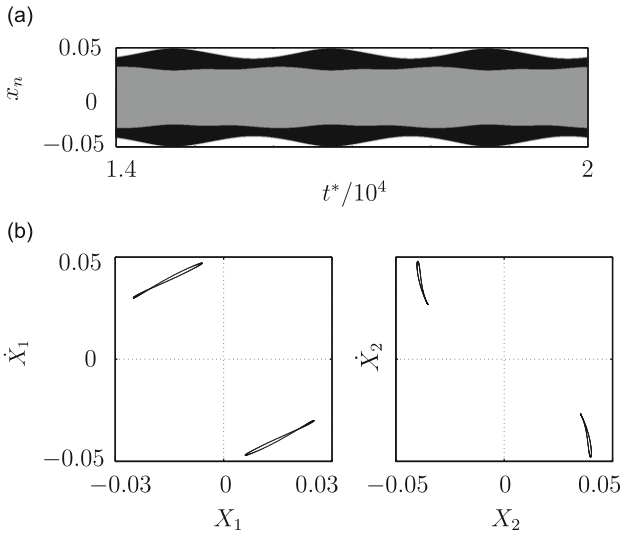

Fig. 10. Simulation in region VII of Fig. 5a ($\Omega = 0.9988\omega$); (a) time series, (b) Poincaré points.

excitation frequency Ω/ω. For clarity, only distinct lines (in most cases m_4=0) are plotted in order to mark the borders between stable and unstable regions. Other distinct lines like m_3=0 or $\Delta_3 = m_3(m_1 m_2 - m_0 m_3) - m_1^2 m_4 = 0$ (criteria for Hopf bifurcation), unless relevant for stability, are not depicted. m_4=0-lines denote a zero eigenvalue ($\lambda_j = 0$) and thus, determine pitchfork bifurcation points with respect to a specific AC-voltage value. In reviewing(39) and (40), there exists a critical AC-voltage value for each solution for which the amplitude square, a_n^2, is equal to zero. This AC-value is represented for each solution by the bold dashed-dotted lines in Fig. 6, respectively. The stability of each solution branch and AC-voltage parameter is investigated by following the grey thin dashed lines in the bifurcation diagrams Fig. 6(0)–(5), respectively. (Fig. 6(0) determines the stability of the trivial solution, which is also indicated by (0) in Fig. 5 but not shown.)

In region I of Fig. 5a there exists one stable trivial solution. In region II (beyond the pitchfork bifurcation) there are two solution branches, the unstable trivial and the stable OOP solution (1) (compare with Fig. 6-1). At the transition from regions II to III, another pitchfork bifurcation point occurs. The unstable trivial solution becomes stable again and an additional unstable branch (2) (which belongs to the OOP-mode) bifurcates from there. The stability of branches (1) and (2) remain unchanged throughout all remaining regions (see Fig. 5a regions I–IX and III–IX, respectively). In region IV the trivial solution is unstable and, in addition to the previous three solutions, a fourth solution exists which corresponds to

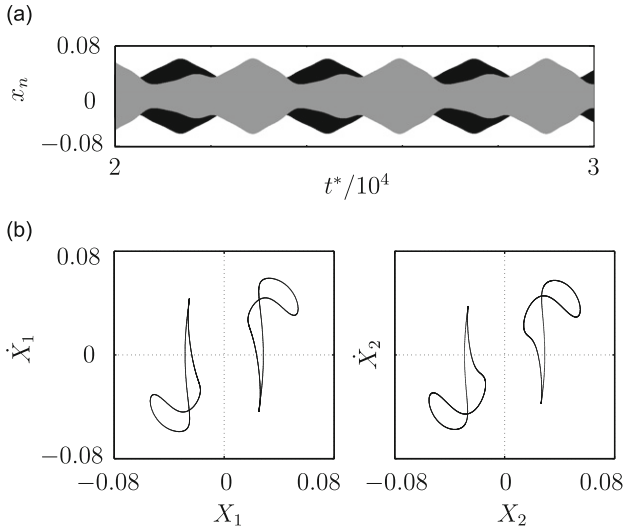

Fig. 11. Simulation in region VII of Fig. 5a ($\Omega = 0.9994\omega$); (a) time series, (b) Poincaré points.

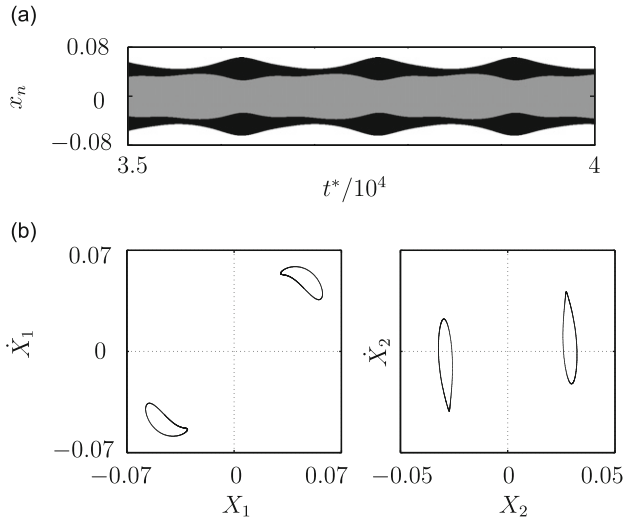

Fig. 12. Simulation in region VIII of Fig. 5a ($\Omega = \omega$); (a) time series, (b) Poincaré points.

the IP mode. Fig. 6-3 reveals that this solution is stable until it loses stability at the transition to region V. Another pitchfork bifurcation point occurs at which the stable IP solution ((3) in region IV) loses stability and two stable branches ($m_k > 0$ for k=[1..4], $\Delta_3 > 0$) emerge ((5) in region V). The trivial solution is unstable in region V. In region VI an additional solution branch (4) appears corresponding to the unstable IP solution. The stability diagram (Fig. 5-4) reveals its instability throughout the remains of all regions. The trivial solution is stable and remains stable throughout region IX. The transition point along solution branch (5) from regions VI to VII is a Hopf bifurcation point, i.e. a pure imaginary set of eigenvalues ($\lambda_j = \pm \mathrm{i}\zeta$) exist. It corresponds to that point in Fig. 6-5, when following the dashed line of $\eta = 0.2354$, of entering the shaded area (Hopf isle) for $\Delta_3 < 0\ \forall m_k > 0$. Stability analysis of this IP-mode solution is determined from Fig. 6-5, which depicts the stability regions in the domain of $\eta = [0.1,0.4]$. Bold grey dots mark distinctive points on the line representing $\Delta_3 = 0$ and bold black dots denote the line of m_4=0. Within the small Hopf isle solutions other than the so far periodic solutions, namely aperiodic solutions, of Eqs. (31)–(34) are expected. At the transition from regions VII to VIII the unstable IP branch (4) intersects with the branch (6). Branch (6) is and remains unstable throughout the remaining regions (VIII–IX). Region IX begins with the second Hopf bifurcation point of solution branch (5). It corresponds to that point in Fig. 6-5 of exiting the Hopf isle again. In region IX solution (5) retains the stability of the limit cycle again.

For larger AC-input values the number of regions in the bifurcation diagram decreases to seven. The observed Hopf points are absent for larger AC-voltage values. A frequency response curve for $\eta = 0.3138$ is presented in Fig. 5b. Note that regions I through V remain the same regardless of occurrence or absence of Hopf bifurcation points.

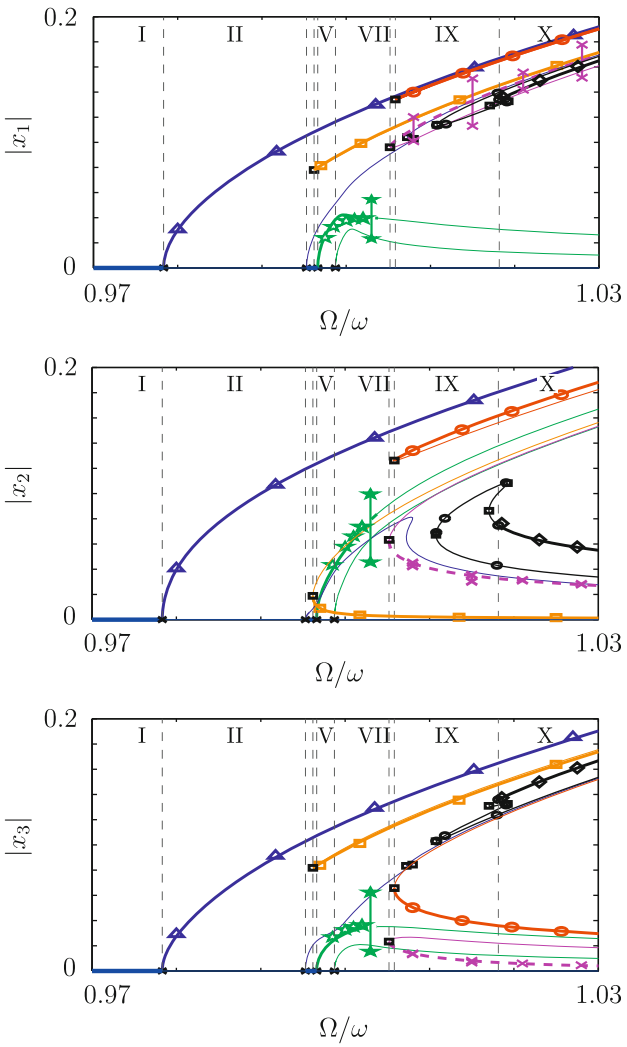

Fig. 13. Frequency response for the three-beam system; $\alpha = 2.8982$, $\beta = 11.5091$, Q=500, $\mu_{NL} = 0$, $\eta = 0.3138$; hollow markers and bold solid lines: periodic response, solid markers and bold dashed lines: aperiodic response; markers are numerical validations: triangles, circles, squares, diamonds, stars and crosses denote different solution types (for periodic responses see Figs. 15 and 16). (For interpretation of the references to color in this figure legend, the reader is referred to the web version of this article.)

4. Numerical analysis

4.1. Validation of periodic asymptotic solutions

In this section the results of the weakly nonlinear asymptotic analysis are validated by numerical integration of 8. Figs. 2 and 5 depict numerical results of the single- and two-beam system. Typical simulations, including time series and phase-plane diagrams with Poincaré points are presented for several initial conditions and regions [43]. Fig. 7a depicts a distinct period doubled response of region II in Fig. 5b, where x_1 and x_2 vibrate with a phase shift of $\pi+2k\pi$. The two Poincaré points in Fig. 7b correspond to principal parametric resonance. Fig. 8 depicts a period doubled response of region IV in Fig. 5b, where the two beams are shown to vibrate with same amplitudes and precisely in-phase. Fig. 9 shows a selected period doubled response of region VII in Fig. 5b, where the two beams vibrate in-phase but with unequal amplitudes.

4.2. Quasi-periodic response of the two-beam system

Figs. 10–12 depict distinct quasi-periodic solutions from regions VII and VIII in Fig. 5a—one towards the beginning, one in the middle and one towards the end of the region. The degree of complexity of the Poincaré figures increases towards the middle of this region. The complex double-loop tori evolve from the two Poincaré points (stable limit cycles) in region VI (Fig. 5a) over single-loop and simpler double-loop tori and back to single-loop tori and two Poincaré points in region IX. We point out that although the fast-frequency signals x_n vibrate in IP-mode, the slow-frequency beats appear to be in

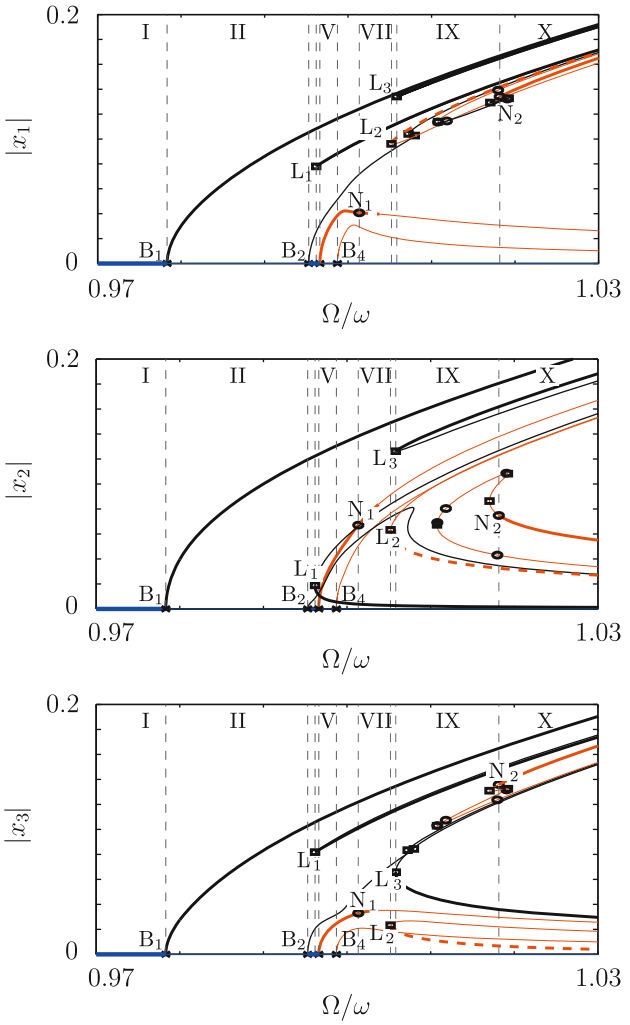

Fig. 14. Frequency response as in Fig. 13; black lines: OOP mode, red lines: IP mode, blue lines: trivial solution; crosses, squares and circles denote bifurcation points: B_i branch points (pitchfork bifurcation), L_i limit points (saddle nodes), N_i Neimark–Sacker (secondary Hopf bifurcation points). (For interpretation of the references to color in this figure legend, the reader is referred to the web version of this article.)

OOP-mode. We conjecture that this is independent of the degree of response complexity but in sync with the one-to-one internal resonance phenomenon of having two vibration modes correspond to one natural frequency.

4.3. Periodic and aperiodic responses of the three-beam system

We now investigate in the dynamic response of a three-beam system by using the numerical continuation method available with the Cl-Matcont package for Matlab [36]. All solution branches were validated by numerically integrating the equations of motion (8) for N=3. The frequency response of the three beams for an AC-value of $\eta = 0.3138$ (and $\alpha = 2.8982$, $\beta = 11.5091$, Q=500, $\mu_{NL} = 0$) is presented in Figs. 13 and 14. Figs. 13 and 14 are identical, but emphasize different findings (denoted by different colors, line styles and the like). While Fig. 13 communicates the number and different types of solutions, Fig. 14 focuses on the bifurcation structure and stability of the same. In the numerical analysis of the three-beam array a total number

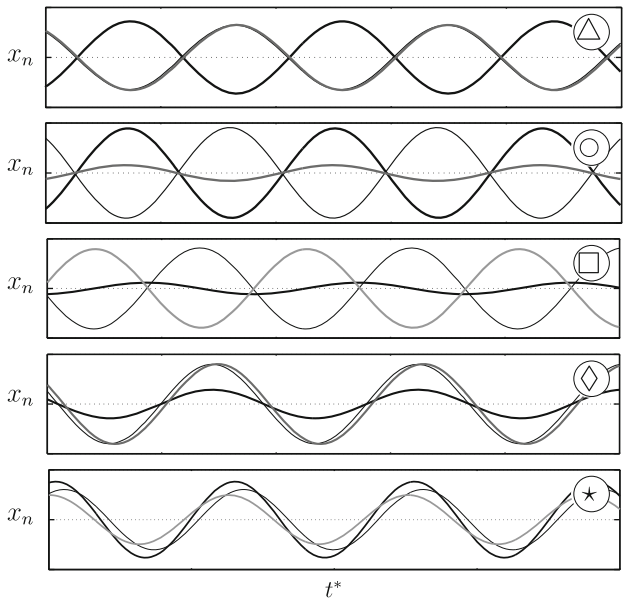

Fig. 15. Time series (steady state) of typical periodic solution types corresponding to Fig. 13; lines: thin black—x_1, bold black—x_2, bold grey—x_3.

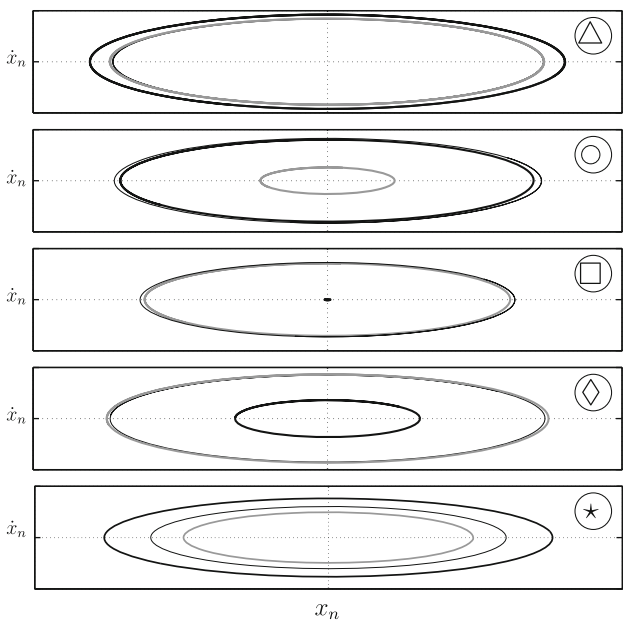

Fig. 16. Phase planes (steady state) of typical periodic solution types corresponding to Figs. 13 and 15; lines: thin black—x_1, bold black—x_2, bold grey—x_3.

of seven solutions are identified, including the trivial, five periodic and one aperiodic solution. The different markers (and colors) in Fig. 13—△, ◦, □, ◇, ⋆, ×—denote various types of solutions, of which periodic responses are depicted in Figs. 15 and 16 (time series and phase plane diagrams, respectively). Hollow markers in Fig. 13 denote periodic and solid markers aperiodic responses, respectively. We find three OOP-mode (△, ◦, □) and two IP-mode (◇, ⋆) periodic solutions.

(△) This solution branch corresponds to the periodic OOP response (see Figs. 15 and 16) and is already known from the two-beam system. It is stable until amplitudes reach a critical amplitude $|x_n| < 0.5$ (for $\Omega \approx 1.105\omega$). Recall that, in the OOP mode, amplitudes of $|x_n| \geq 0.5$ correspond to penetration of neighbor beams and thus, render the dynamical system invalid.

(◦) This solution branch is the second periodic OOP response, where beams vibrate with unequal amplitudes.

(□) This third periodic OOP solution is characterized by the OOP motion of the two outer beams (same amplitudes) while the motion of the middle beam (smaller amplitude) is phase-shifted in time by $\pi/2$.

(◇) This solution presents one of the two periodic in-phase responses. The two outer beams vibrate with similar amplitudes while the middle beam carries on with a smaller amplitude.

(⋆) The second IP solution is characterized by the vibration of all beams with a similar amplitude and a slight phase shift.

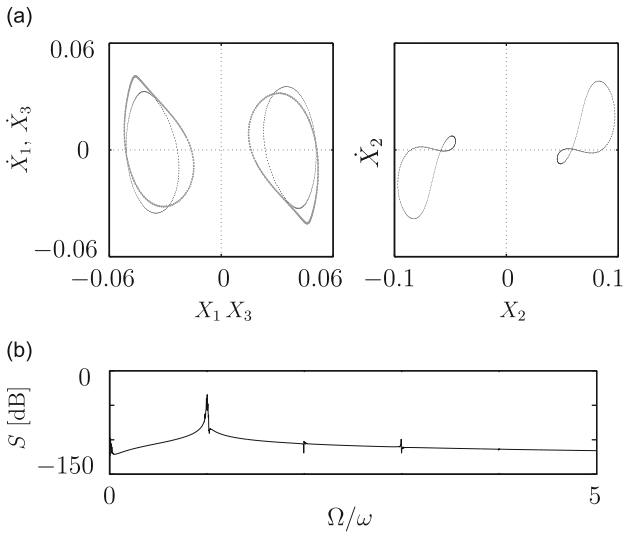

Fig. 17. Simulation of the aperiodic ⋆- solution (of Fig. 13) at $\Omega = 1.003\omega$, (a) Poincaré points, (b) power spectrum.

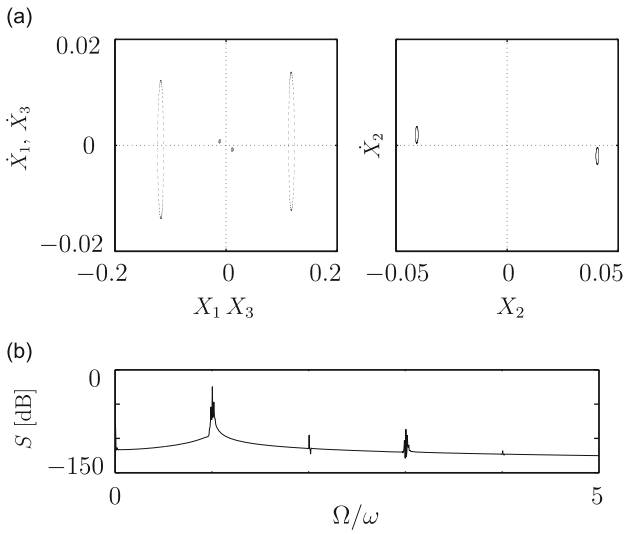

Fig. 18. Simulation of the aperiodic × -solution (of Fig. 13) at $\Omega = 1.01\omega$, (a) Poincaré points, (b) power spectrum.

While the $\star$ solution is periodic in regions V and VI (see Fig. 13), the limit cycles lose stability in regions VII and following. A selected simulation of this vibration mode at $\Omega = 1.003\omega$ is depicted in Fig. 17. Its response is quasi-periodic. Another solution is identified in the three-beam analysis, which corresponds to a quasi-periodic solution, denoted by $\times$ in Fig. 13. A selected simulation at $\Omega = 1.01\omega$ is shown in Fig. 18. The largest amplitude corresponds to one of the outer beams, followed by the middle and a yet smaller amplitude for the third beam.

Fig. 14 depicts the bifurcation structure of the three-beam system and the stability of solutions. The previously analyzed bifurcation types of the two-beam system are also identified in the analysis of the three-beam array. Crosses, squares and circles in Fig. 14 denote branch, limit and Neimark–Sacker point bifurcations, respectively. The branch point bifurcations (indicated by B_i for i=1,2,…) are pitchfork bifurcation points, at which solutions intersect. A limit point (L_i) in the Cl-Matcont continuation solver denotes that which is a saddle-node bifurcation of the equilibrium while a Neimark–Sacker point (N_i) corresponds to a secondary Hopf bifurcation (which is a Hopf point in the slowly varying evolution equations). The number of bifurcation points determines the different types of array behavior (divided by regions I–X in Fig. 14). Note that only bifurcation points which reveal a change in behavior (and are validated by simulations) have been labeled. Bold blue, black and red solid lines in Fig. 14 denote the stable trivial and the periodic OOP- and IP-mode solution branches, respectively, while bold dashed lines indicate quasi-periodic solutions (compare with Figs. 13, 17, 18). For the two- as well as three-beam array, aperiodic responses occur for the IP-mode solution(s). The three-beam analysis (in the presented domain) of the $\times$ solution reveals that this aperiodic solution does neither evolve from nor to a periodic solution like in the case of the two-beam system.

5. Conclusions

In this paper we have derived a nonlinear multi-element dynamical system for a microbeam array subject to electrodynamic parametric excitation. The reduced-order model is derived from a consistent continuum-based formulation which assures the assignment of all linear and nonlinear parameters to physical meanings of the real microbeam array. An asymptotic multiple-scales analysis for a two-element system near the one-to-one internal resonance reveals the existence of multiple coexisting periodic in- and out-of-phase solutions with equal and unequal amplitudes as well as quasi-periodic solutions that emerge when a periodic in-phase response loses stability. A comprehensive stability analysis enables derivation of the system bifurcation structure which incorporates multiple distinct regions with different behavior. The governing parameters controlling the bifurcation structure are the nondimensional oscillating excitation and linear damping coefficient which determine the number of regions in the bifurcation diagram.

The conclusions from analysis of the two- and the three-beam systems enable understanding of the dynamical behavior of neighbor elements in multi-microbeam arrays. We conclude that the out-of-phase solutions are stable and periodic up to amplitudes near penetration of neighbor beams and that solutions that bifurcate from an in-phase solution were found to be candidates for aperiodic responses. In the case of an aperiodic response, the fast-frequency signals of each beam vibrate in-phase while the slow-frequency signals (beats) vibrate out-of-phase. The complexity of the periodic system response is determined by the respective Poincaré maps which depend on the amplitude of each beam and the number of beams in the array.

Acknowledgments

This work was supported by the Israeli Science Foundation, the Vatat (Council for Higher Education) and the Minerva for which we express our thanks. S.G. would like to thank the people in the Mechanical Engineering Department at Technion—Israel Institute of Technology, Haifa (Israel) for their hospitality during the postdoctoral years.

Appendix A. Single-beam system implementing two modes

We investigate the dynamic behavior of the single-beam system considering the first two symmetric eigenmodes of the resonator. The nondimensional field equation for the single-beam system (N=1) is given in (1). We, henceforth, concentrate on terms that are essential to the purpose of this exercise, and thus, neglect the nonlinear damping term which is only of importance for assuring finite amplitudes. Separation of variables is applied with

$$w(s,\tau) = \sum_{j=1}^{2} q_j(\tau)\Phi_j(s) = q_1\Phi_1 + q_2\Phi_2. \tag{A.1}$$

We substitute $w(s,\tau)$ into (1) and employ Galerkin's method by multiplication of Φ_j and integration by parts over the length of the beam (from 0 to 1), which yields the set of nonlinear coupled ordinary differential equations

$$\mathbf{J}_M\mathbf{q}_{\tau\tau} + \mathbf{J}_C\mathbf{q}_{\tau} + (\mathbf{J}_{Kl} + \mathbf{J}_{Knl})\mathbf{q} = \Gamma V_{AC}^2\mathbf{f}. \tag{A.2}$$

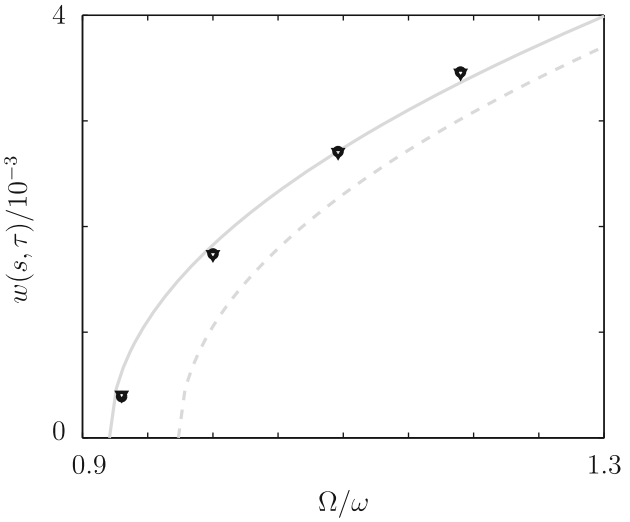

Fig. 19. Frequency responses of the single-beam system with implementations of single- and two-(symmetric) mode approximation; circles: single-mode approximation (simulation), grey lines: single-mode (analytical), triangles: two-mode approximation (simulation); $\alpha = 2.8982$, $\beta = 11.5091$, Q=500, $\eta = 0.4600$, $\mu_{NL} = 0$.

In (A.2) $\mathbf{q}=\{q_1, q_2\}^T$ is the time dependent vector of generalized coordinates, $\mathbf{J}_M=[m_{ij}]$, $\mathbf{J}_C=[c_{ij}]$, $\mathbf{J}_{Kl}=[kl_{ij}]$ are mass, damping, and linear stiffness matrices, respectively, with

$$m_{jj} = \int_0^1 \Phi_j^2 \,\mathrm{d}s, \quad c_{jj} = \mu_L m_{jj}, \quad kl_{jj} = \int_0^1 [\Phi_{j,ss}^2 + \kappa_1 \Phi_{j,s}^2] \,\mathrm{d}s. \tag{A.3}$$

The nonlinear stiffness matrix in (A.2) is $\mathbf{J}_{Knl}=[knl_{ij}]$ with

$$knl_{ij} = \kappa_3 \sum_{k,l=1}^{2} q_k q_l \int_0^1 \Phi_{k,s}\Phi_{l,s} \,\mathrm{d}s \int_0^1 \Phi_{i,s}\Phi_{j,s} \,\mathrm{d}s. \tag{A.4}$$

The actuation term in (A.2) is

$$\mathbf{f} = \hat{\Gamma} V_{AC}^2 \frac{4\gamma \sum_{k=1}^{2} q_k \overline{\Phi}_k}{(\gamma^2 - [\sum_{k=1}^{2} q_k \overline{\Phi}_k]^2)^2} \cdot \{\overline{\Phi}_1, \overline{\Phi}_2\}^T, \tag{A.5}$$

with $\overline{\Phi}_k = \Phi_k(1/2)$ being the values of the modeshapes at midspan of the resonator, respectively, and γ is the scaled gap parameter.

Numerical integration of (A.2) at various excitation frequencies near the principal parametric resonance yields the frequency response plot depicted in Fig. 19. In addition to the result containing two modes, Fig. 19 portrays the corresponding results of analytical as well as numerical results of the single mode analysis. The relative error between the single- and two-mode analysis is less than one percent and thus, an analysis using only first modes of each resonators, respectively, is justified.

Appendix B. Step-by-step derivation of Eq. (19) from (18)

Recalling (18)

$$\delta_{\mathrm{ex}}^2 = (2\zeta_L + 2\zeta_{NL}a^2)^2 + (\delta_3 a^2 - 2\sigma - 2\delta_{\mathrm{ex}})^2.$$

Multiplying (18) by ε^4 yields

$$\varepsilon^4\delta_{\mathrm{ex}}^2 = (2\varepsilon^2\zeta_L + 2\zeta_{NL}\varepsilon^2 a^2)^2 + (\delta_3\varepsilon^2 a^2 - 2\varepsilon^2\sigma - 2\varepsilon^2\delta_{\mathrm{ex}})^2. \tag{B.1}$$

Sorting (B.1) and collecting terms in $\varepsilon^2\sigma$ results in

$$\varepsilon^4\sigma^2 - (\delta_3\varepsilon^2 a^2 - 2\varepsilon^2\delta_{\mathrm{ex}})\varepsilon^2\sigma + \frac{1}{4}(\delta_3\varepsilon^2 a^2 - 2\varepsilon^2\delta_{\mathrm{ex}})^2 + \frac{1}{4}(2\varepsilon^2\zeta_L + 2\zeta_{NL}\varepsilon^2 a^2)^2 - \frac{1}{4}\varepsilon^4\delta_{\mathrm{ex}}^2 = 0. \tag{B.2}$$

Eq. (B.2) is a quadratic equation in $\varepsilon^2\sigma$, whose solutions are

$$(\varepsilon^2\sigma)_{1,2} = \frac{1}{2}\delta_3\varepsilon^2 a^2 - \varepsilon^2\delta_{\mathrm{ex}} \pm \frac{1}{2}\sqrt{(\varepsilon^2\delta_{\mathrm{ex}})^2 - (2\varepsilon^2\zeta_L + 2\zeta_{NL}\varepsilon^2 a^2)^2}. \tag{B.3}$$

Finally, substituting former definitions $\zeta_L=\overline{\mu}_L/2$, $\zeta_{NL}=\mu_{NL}/8$, $\delta_{\mathrm{ex}}=\overline{\eta}^2/(4\omega)$, unscaled parameters $\eta=\varepsilon\overline{\eta}$, $\mu_L=\varepsilon^2\overline{\mu}_L$ and the detuning $\varepsilon^2\sigma=\Omega-\omega$ back into (B.3) results in

$$\Omega_{1,2}=\frac{1}{2}\delta_3\varepsilon^2a^2-\frac{\eta^2}{4\omega}\pm\frac{1}{2}\sqrt{\frac{\eta^4}{16\omega^2}-\left(\mu_L+\frac{\mu_{NL}}{4}\varepsilon^2a^2\right)^2}+\omega, \tag{B.4}$$

which is Eq. (19).

Appendix C. Step-by-step derivation of constraint (37) from (35)

The condition for which the amplitude square, a^2, is greater than zero is determined from solutions (35)

$$\delta_{\mathrm{ex}}^2=(4\zeta_L+2\zeta_{NL}a^2)^2+(2\delta_3a^2-4\sigma-2\delta_{\mathrm{ex}})^2$$

by differentiating the same with respect to σ and setting $\mathrm{d}a/\mathrm{d}\sigma$ equal to zero, which results in

$$-8(2\delta_3a^2-4\sigma_E-2\delta_{\mathrm{ex}})=0.$$

Substituting the local extremum σ_E,

$$\sigma_E=\frac{\delta_3a^2-\delta_{\mathrm{ex}}}{2}$$

into (35), and solving for a^2 yields

$$a_{\min}^2\geq\frac{\delta_{\mathrm{ex}}-4\zeta_L}{2\zeta_3},$$

which is the constraint (37). Analogous steps beginning from (36) yield to the constraint (38).

References

[1] B. Ilic, Y. Yang, K. Aubin, R. Reichenbach, S. Krylov, H. Craighead, Enumeration of DNA molecules bound to a nanomechanical oscillator, *Nano Lett.* 5 (5) (2005) 925–929.
[2] M. Zalalutdinov, J. Baldwin, M. Marcus, R. Reichenbach, J. Parpia, B. Houston, Two-dimensional array of coupled nanomechanical resonators, *Appl. Phys. Lett.* 88 (2006) 143504.
[3] M. Despont, U. Drechsler, R. Yu, H. Pogge, P. Vettiger, Wafer-scale microdevice transfer/interconnect: its application in an AFM-based data-storage system, *J. Microelectromech. Syst.* 13 (6) (2004) 895–901.
[4] M. Sato, B. Hubbard, A. Sievers, Colloquium: nonlinear energy localization and its manipulation in micromechanical oscillator arrays, *Rev. Mod. Phys.* 78 (1) (2006) 137–157.
[5] P. Vettiger, J. Brugger, M. Despont, U. Drechsler, U. Dürig, W. Häberle, M. Lutwyche, H. Rothuizen, R. Stutz, R. Widmer, G. Binnig, Ultrahigh density, high-data-rate NEMS-based AFM data storage system, *Appl. Phys. Lett.* 46 (1–4) (1999) 11–17.
[6] M. Baller, H. Lang, J. Fritz, C. Gerber, J. Gimzewski, U. Drechsler, H. Rothuizen, M. Despont, P. Vettiger, F. Battiston, J. Ramseyer, P. Fornaro, E. Meyer, H.-J. Güntherodt, A cantilever array-based artificial nose, *Ultramicroscopy* 82 (2000) 1–9.
[7] C. Britton Jr., R. Jones, P. Oden, Z. Hu, R. Warmack, S. Smith, W. Bryan, J. Rochelle, Multiple-input microcantilever sensors, *Ultramicroscopy* 82 (2000) 17–21.
[8] E. Buks, M. Roukes, Electrically tunable collective response in a coupled micromechanical array, *J. Microelectromech. Syst.* 11 (6) (2002) 802–807.
[9] M. Napoli, W. Zhang, K. Turner, B. Bamieh, Characterization of electrostatically coupled microcantilevers, *J. Microelectromech. Syst.* 14 (2) (2005) 295–304.
[10] P.-F. Indermühle, G. Schürmann, G.-A. Racine, N. de Rooij, Fabrication and characterization of cantilevers with integrated sharp tips and piezoelectric elements for actuation and detection for parallel AFM applications, *Sensors Actuators A Phys.* 60 (1–3) (1997) 186–190.
[11] Y. Sarov, T. Ivanov, A. Frank, I. Rangelow, Controllable off-plane deflection of cantilevers for multiple scanning proximity probe arrays, *Appl. Phys. A* 92 (2008) 525–530.
[12] F. Sasoglu, A. Bohl, B. Layton, Design and microfabrication of a high-aspect-ratio PDMS microbeam array for parallel nanonewton force measurement and protein printing, *J. Micromech. Microeng.* 17 (3) (2007) 623–632.
[13] E. Kenig, B. Malomed, M. Cross, R. Lifshitz, Intrinsic localized modes in parametrically driven arrays of nonlinear resonators, *Phys. Rev. E* 80 (2009) 046202.
[14] Y. Bromberg, M. Cross, R. Lifshitz, Response of discrete nonlinear systems with many degrees of freedom, *Phys. Rev. E* 73 (2006) 016214.
[15] A. Dick, B. Balachandran, C. Mote Jr., Intrinsic localized modes in microresonator arrays and their relationship to nonlinear vibration modes, *Nonlinear Dyn.* 54 (1–2) (2008) 13–29.
[16] A. Dick, B. Balachandran, C. Mote Jr., Localization in microresonator arrays: influence of natural frequency tuning, *J. Comput. Nonlinear Dyn.* 5 (2010) 011002.
[17] S. Minne, S. Manalis, C. Quate, *Bringing Scanning Probe Microscopy up to Speed*, Kluwer Academic, Boston, 1999.
[18] R. Lifshitz, M. Cross, Response of parametrically driven nonlinear coupled oscillators with application to micromechanical and nanomechanical resonator arrays, *Phys. Rev. B* 67 (2003) 134302.
[19] A. Dick, B. Balachandran, C. Mote Jr., Intrinsic localized modes and nonlinear normal modes in micro-resonator arrays, *Proceedings of IMECE 2005*, Orlando, FL, USA, November 5–11, 2005.
[20] W. Zhang, K. Turner, Frequency dependent fluid damping of micro/nano flexural resonators: experiment, model and analysis, *Sensors Actuators A* 134 (2007) 594–599.
[21] S. Gutschmidt, O. Gottlieb, Nonlinear internal resonances of a microbeam array near the pull-in point, *Proceedings of 6th EUROMECH Nonlinear Dynamics Conference*, St. Petersburg, Russia, June 30–July 4, 2008.
[22] S. Gutschmidt, O. Gottlieb, Numerical analysis of a three element microbeam array subject to electrodynamical parametric excitation, *Proceedings of ASME/ESDA 2008*, Haifa, Israel, July 7–9, 2008.
[23] H. Nathanson, W. Newell, R. Wickstrom, J. Davis Jr., The resonant gate transistor, *IEEE Trans. Electron Devices* 14 (1967) 117–133.
[24] S. Senturia, *Microsystem Design*, Kluwer Academic Publishers, Boston, 2001.
[25] S. Lenci, G. Rega, Control of pull-in dynamics in a nonlinear thermoelastic electrically actuated microbeam, *J. Micromech. Microeng.* 16 (2006) 390–401.

[26] P. Wang, Bifurcation of equilibrium in micromachined elastic structures with liquid interface, *Int. J. Bifurcation Chaos* 13 (2003) 1019–1027.
[27] A. Nayfeh, M. Younis, E. Abdel-Rahman, Dynamic pull-in phenomenon in MEMS resonators, *Nonlinear Dyn.* 48 (2007) 153–163.
[28] R. Batra, M. Porfiri, D. Spinello, Vibrations and pull-in instabilities of microelectromechanical von Kármán elliptic plates incorporating the Casimir force, *J. Sound Vib.* 309 (2008) 600–612.
[29] C. Berli, A. Cardona, On the calculation of viscous damping of microbeam resonators in air, *J. Sound Vib.* 327 (2009) 249–253.
[30] M. Porfiri, Vibrations of parallel arrays of electrostatically actuated microplates, *J. Sound Vib.* 315 (2008) 1071–1085.
[31] A. Nayfeh, D. Mook, *Nonlinear Oscillations*, Wiley-Interscience, New York, 1979.
[32] A. Nayfeh, *Nonlinear Interactions*, Wiley-Interscience, New York, 2000.
[33] R. Karabalin, M. Cross, M. Roukes, Nonlinear dynamics and chaos in two coupled nanomechanical resonators, *Phys. Rev. B* 79 (2009) 165309.
[34] P. Wang, Feedback control of vibrations in a micromachined cantilever beam with electrostatic actuators, *J. Sound Vib.* 213 (2) (1998) 537–550.
[35] E. Allgower, K. Georg, *Numerical Continuation Methods: An Introduction*, Springer-Verlag, Berlin, 1990.
[36] W. Govaerts, Y. Kuznetsov, A. Dhooge, Numerical continuation of bifurcations of limit cycles in MATLAB, *SIAM J. Sci. Comput.* 27 (2005) 231–252.
[37] L. Meirovitch, *Elements of Vibration Analysis*, McGraw-Hill, New York, 1975.
[38] A. Shabana, *Theory of Vibration*, Springer-Verlag, New York, 1991.
[39] O. Gottlieb, A. Champneys, Global bifurcations of nonlinear thermoelastic microbeams subject to electrodynamic actuation, *IUTAM Chaotic Dynamics and Control of Systems and Processes in Mechanics*, Springer, Rome, Italy, 2005, pp. 117–126.
[40] P. Hagedorn, A. DasGupta, *Vibrations and Waves in Continuous Mechanical Systems*, Wiley & Sons, Chichester, 2007.
[41] S. Krylov, Lyapunov exponents as a criterion for the dynamic pull-in instability of electrostatically actuated microstructures, *Int. J. Nonlinear Mech.* 42 (2007) 626–642.
[42] J. Rhoads, S. Shaw, K. Turner, The nonlinear response of resonant microbeam systems with purely-parametric electrostatic actuation, *J. Micromech. Microeng.* 16 (2006) 890–899.
[43] M. Leamy, O. Gottlieb, Internal resonances in whirling strings involving longitudinal dynamics and material non-linearities, *J. Sound Vib.* 236 (4) (2000) 683–703.